Electronic Raman scattering and the Fano resonance in metallic carbon nanotubes

Eddwi H. Hasdeo,[1,*] Ahmad R. T. Nugraha,[1] Kentaro Sato,[1,4] Mildred S. Dresselhaus,[2,3] and Riichiro Saito[1]

[1]*Department of Physics, Tohoku University, Sendai 980-8578, Japan*

[2]*Department of Physics, Massachusetts Institute of Technology, Cambridge, Massachusetts 02139-4307, USA*

[3]*Department of Electrical Engineering and Computer Science, Massachusetts Institute of Technology, Cambridge, Massachusetts 02139-4307, USA*

[4]*Sendai National College of Technology, Sendai 989-3128, Japan*

The Fano resonance spectra for the G band in metallic carbon nanotubes are calculated as a function of laser excitation energy, in which the origin of the resonance is given by an interference between the continuous electronic Raman spectra and the discrete phonon spectra. We found that the second-order scattering process of the $\mathbf{q} \neq 0$ electron-electron interaction is more relevant to the continuous spectra rather than the $\mathbf{q} = 0$ first-order process because the $\mathbf{q} = 0$ direct Coulomb interaction vanishes due to the symmetry of the two sublattices of a carbon nanotube.

I. INTRODUCTION

Raman spectroscopy of single-wall carbon nanotubes (SWNTs) and graphene has provided us with a better understanding of many optical properties, which are important for characterizing SWNTs and graphene, not only for basic science understanding but also in applications.[1] In particular, most of the excitonic physics in the Raman spectra of SWNTs has been investigated intensively in terms of, for example, the excitation energy dependence (resonance Raman effect),[2,3] the chirality dependence (the Kataura plot),[4–6] the Fermi energy dependence (the Kohn anomaly),[7–9] the polarization dependence,[10–12] and even the strain dependence.[13,14] However, the origin of the Fano resonance in metallic SWNTs (mSWNTs), indicated by the presence of a Breit-Wigner-Fano (BWF) lineshape (which is an asymmetric lineshape) in the G band ($\sim$1600 cm^{-1})[1] of mSWNTs, is still not well-explained theoretically. In a previous study, Brown *et al.* showed the diameter (d_t)-dependent asymmetric spectral lineshape of the G band, in which the asymmetric factor $1/q_{\mathrm{BWF}}$ depends on the density of states at the Fermi energy.[15] Additionally, the BWF line shapes appear in graphite intercalation compounds (GICs), where the $1/q_{\mathrm{BWF}}$ factor depends on the staging number of GICs and thus also depends on the density of states at the Fermi energy.[16] Therefore, electrons in the gapless linear energy band of mSWNTs should be expected to exhibit these same asymmetry-related phenomena, and this asymmetry in the G band of mSWNTs will be the main focus of this paper.

In the early 1960s, Fano pointed out that the asymmetric feature of a broadened spectrum comes from an interference between a discrete excitation spectrum and a continuum spectrum.[17] Now, in our discussion of mSWNTs, electrons in the linear energy band may play an important role in giving rise to the continuum spectra, while phonons give discrete spectra. However, the detailed mechanism of the BWF line shapes in mSWNTs remains a long-standing debatable topic. Some reports suggest that the coupling of a collective excitation (plasmon) with a phonon could explain the origin of the BWF asymmetry,[15,18–20] and some others argue that the single-particle electron-hole pair and phonon coupling via the Kohn anomaly are more relevant.[21,22] Recently, Farhat

et al. have observed a new feature of the continuum spectra exclusively in mSWNTs, which is ascribed to the electronic Raman scattering (ERS).[23] The ERS feature (at $\sim$500 cm^{-1}) is observed in the energy region between the radial breathing mode (RBM)[1] at $\sim$200 cm^{-1} and the G band ($\sim$1600 cm^{-1}). It also shows no phonon-related feature based on the following arguments: (1) in comparison to the phonon spectral width ($\sim$1–50 cm^{-1}), the ERS width is much broader ($\sim$500 cm^{-1}) and has a smaller peak intensity ($I_{\mathrm{ERS}} \approx 0.6 I_G$); (2) the energy of the inelastic scattered light ($\hbar\omega_s$) in the phonon Raman spectra increases linearly by increasing the laser excitation energy E_L, while the ERS peak position does not change—it remains constant at M_{ii} (the ith Van Hove singularity transition energy); and (3) the ERS feature is suppressed by changing the Fermi energy, which indicates that the origin of this spectrum comes from electron-hole pair excitations in the linear band of mSWNTs by the Coulomb interaction.

In this work, we propose that the BWF feature of mSWNTs comes from the interference between the G band and the ERS spectra. We calculate the exciton-exciton interaction matrix elements, which are responsible for the experimental observation of the ERS spectra. Based on the fact that exciton effects in mSWNTs are not negligible due to the one-dimensional carrier confinement even in the presence of the screening effect,[24,25] the electron-hole pair excitations in mSWNTs should be described by exciton wave functions. In parabolic energy bands of mSWNTs, excitons can exist with a binding energy $\sim$50 meV, and even in a linear energy band, the exciton binding energy from calculation is found to be $\sim$10 meV, which is of the same order of magnitude as the ERS energy and thus the exciton effect cannot be neglected.[6] From the calculated results of the present work, we found that the zero momentum transfer ($\mathbf{q} = 0$) vanishes in the direct Coulomb interaction because of the symmetry of the two sublattices in a graphene unit cell, which is a building block of the SWNT's unit cell. This finding holds in the general case, not only for carbon sp^2 systems, but also for other materials that have the same symmetry. This fact also implies that a higher-order Raman process is relevant to the ERS phenomenon. By considering the second-order Raman
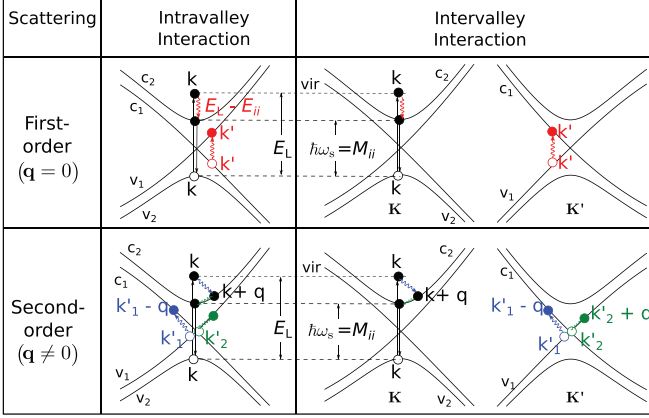
FIG. 1. (Color online) Electronic Raman scattering (ERS) may occur in terms of first-order processes or second-order processes, and intravalley interactions (AV) or intervalley interactions (EV). For simplicity, we only draw the direct Coulomb interactions in this diagram, while the exchange Coulomb interaction processes are shown in Figs. 2(b) and 2(c). In EV, the interaction between the photoexcited carrier in the parabolic band and the electron(s) in the linear band takes place in different valleys (K and K' points). It should be noted that we do not consider a direct Coulomb interaction with a large momentum transfer $\mathbf{q}$ connecting the K and K' points, because its matrix element is two orders of magnitude smaller than that of $\mathbf{q}$ within the same valley [compare the direct interaction described in the legend of Fig. 2(d) with the exchange interaction described in the legend of Fig. 2(e) for the EV case].

process, we are able to reproduce the experimental results of the ERS spectra systematically.

II. THEORETICAL METHOD

Optical processes of the ERS are described in Fig. 1 and consist of (i) an exciton generation via an exciton-photon interaction, (ii) excitation of another exciton in the linear energy band by the Coulomb interaction with the photoexcited exciton, and (iii) finally, the photoexcited exciton goes back to the ground state by emitting a photon. The exciton-exciton interaction in (ii) may occur in either first-order or high-order processes. Here, we consider up to second-order processes for simplicity. For the first-order process, the photoexcited exciton relaxes vertically ($\mathbf{q} = 0$) from a virtual state Ψ^{vir} to the M_{ii} state after photoabsorption at a wave vector $\mathbf{k}$, while the other exciton is created in the linear band at wave vector $\mathbf{k}'$ by the Coulomb interaction. In the second-order process, the photoexcited exciton is scattered twice by transferring momentum $\mathbf{q}$ and $-\mathbf{q}$ by creating two excitons in the linear band. Due to the existence of two gapless energy bands (the Dirac cones) in two inequivalent K and K' points in the graphene Brillouin zone, both the first-order and the second-order processes always have two cases where the electrons in the parabolic and linear bands may exist in the same valley (AV intravalley interaction), or they may exist in different valleys (EV intervalley interaction). After going through the electronic scattering process, the photoexcited exciton then returns to the ground state by emitting a photon with resonance energy $\hbar\omega_s = M_{ii}$. This is the reason why the ERS peak remains at M_{ii}, even though we change the laser energy E_L.

Considering all the processes shown in Fig. 1, we write the perturbed Hamiltonian as

$$H_{e\text{-}e} = \sum_{\mathbf{k},\mathbf{k}',\mathbf{q}} W^{(\pm)}_{\mathbf{k}+\mathbf{q},\mathbf{k}'-\mathbf{q},\mathbf{k},\mathbf{k}'} c^{\dagger c}_{\mathbf{k}+\mathbf{q}} c^{\dagger c'}_{\mathbf{k}'-\mathbf{q}} c^{v'}_{\mathbf{k}'} c^{c}_{\mathbf{k}}, \qquad (1)$$

where $\mathbf{k}$ and $\mathbf{k}'$ denote, respectively, an electron state in the parabolic and the linear band, while $c^{\dagger c}_{\mathbf{k}}(c^{v}_{\mathbf{k}})$ is the creation (annihilation) operator in the conduction (valence) band. Although there are many other Coulomb interaction processes, we only consider those processes described by Eq. (1), which are responsible for the ERS spectra. The rest of the Coulomb interaction has already been taken into account in the exciton calculation.[6] The direct (exchange) interaction K^d (K^x) contributes to the two-body Coulomb interaction W as follows: $W^{(\pm)} = K^d \pm K^x$, in which $+(-)$ gives a singlet (triplet) state for the two electrons. K^d and K^x are expressed as (see Appendix A for the details):

$$K^d = \sum_{ss'=A,B} C^{c*}_{s,\mathbf{k}+\mathbf{q}} C^{c*}_{s',\mathbf{k}'-\mathbf{q}} C^{c}_{s,\mathbf{k}} C^{v}_{s',\mathbf{k}'} \mathrm{Re}[w_{ss'}(\mathbf{q})], \qquad (2)$$

$$K^x = \sum_{ss'=A,B} C^{c*}_{s,\mathbf{k}+\mathbf{q}} C^{c*}_{s',\mathbf{k}'-\mathbf{q}} C^{c}_{s',\mathbf{k}} C^{v}_{s,\mathbf{k}'} \mathrm{Re}[w_{ss'}(\mathbf{k}'-\mathbf{k}-\mathbf{q})],$$

$$\qquad (3)$$

where $C^{c(v)}_{s,\mathbf{k}}$ are the tight-binding coefficients for $s = A$ or B atomic sites of the conduction (valence) band, and the screened potential $w(\mathbf{q})$ is given by the random phase approximation (RPA): $w(\mathbf{q}) = v(\mathbf{q})/\kappa[1 + v(\mathbf{q})\Pi(\mathbf{q})]$.[6,12] Here $v(\mathbf{q})$ denotes the Fourier transform of the Ohno potential, $\Pi(\mathbf{q})$ is the RPA polarization function, and κ is the static dielectric constant due to electronic core states, σ bands, and the surrounding material. In this calculation we use a constant $\kappa = 2.2$.[6]

The exciton-exciton matrix element for the photoexcited exciton and another exciton in a linear energy band is calculated using the following formula:

$$\begin{aligned}
\mathcal{M}^{\pm}_{\mathrm{ex\text{-}ex}}(\mathbf{q}) &= \langle \Psi^f | H_{e\text{-}e} | \Psi^{\mathrm{vir}} \rangle \\
&= \sum_{\mathbf{k},\mathbf{k}'} Z^*_{(\mathbf{k}+\mathbf{q})c,\mathbf{k}v} Z^*_{(\mathbf{k}'-\mathbf{q})c,\mathbf{k}'v} Z_{\mathbf{k}c,\mathbf{k}v} W^{(\pm)}_{\mathbf{k}+\mathbf{q},\mathbf{k}'-\mathbf{q},\mathbf{k},\mathbf{k}'}.
\end{aligned}$$

$$\qquad (4)$$

Here the photoexcited exciton state is defined by

$$|\Psi^{\mathrm{vir}}\rangle = \sum_{\mathbf{k}} Z^{n=0}_{\mathbf{k}c,\mathbf{k}v} c^{\dagger c}_{\mathbf{k}} c^{v}_{\mathbf{k}} |g\rangle, \qquad (5)$$

where $Z^{n*}_{\mathbf{k}_c,\mathbf{k}_v}$ is the eigenvector of the nth exciton state solved from the Bethe-Salpeter equation, $\mathbf{k}_c$ and $\mathbf{k}_v$ denote wave vectors for the electron and hole states, respectively, with $\mathbf{k}_c = \mathbf{k}_v$ for a bright exciton, and $|g\rangle$ denotes the ground state.[6] In Eq. (5), we only use the lowest exciton state $n = 0$, since it gives the dominant contribution to the Raman spectra (see Appendix B). The final state of Eq. (4) is given by

$$|\Psi^f\rangle = \sum_{\mathbf{k},\mathbf{k}'} Z_{(\mathbf{k}+\mathbf{q})c,\mathbf{k}v} Z_{(\mathbf{k}'-\mathbf{q})c,\mathbf{k}'v} c^{\dagger c}_{\mathbf{k}+\mathbf{q}} c^{\dagger c}_{\mathbf{k}'-\mathbf{q}} c^{v}_{\mathbf{k}'} c^{v}_{\mathbf{k}} |g\rangle. \qquad (6)$$

In Figs. 2(a)–2(c), we schematically illustrate the direct and the exchange Coulomb interaction processes for the AV and EV interactions. We show the separate contributions from K^d and K^x in $\mathcal{M}^{\pm}_{\mathrm{ex\text{-}ex}}$ of Eq. (4) for a (23,14) mSWNT, respectively, in Figs. 2(d) and 2(e). Surprisingly, we find
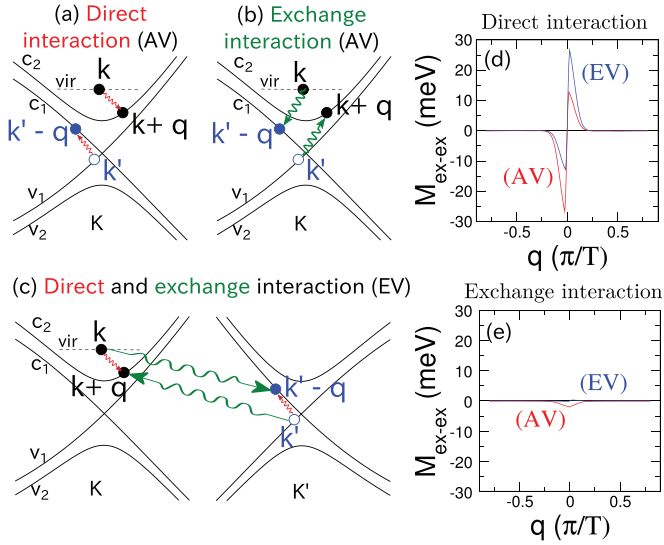
FIG. 2. (Color online) (a) The direct (AV), (b) the exchange (AV), and (c) the direct (red) and exchange (green) (EV) Coulomb interaction process. (d) and (e) contribution from the direct Coulomb interaction [Eq. (2)] and the exchange Coulomb interaction [Eq. (3)], respectively, in the exciton-exciton matrix element $\mathcal{M}_{\mathrm{ex\text{-}ex}}^{\pm}$ [Eq. (4)] of a (23,14) tube ($d_t = 2.53$ nm). The label AV (EV) inside each panel shows the states, in which two electrons lie in the same (different) valley. The one-dimensional (1D) wave vector $\mathbf{q}$ is projected on the 1D SWNT cutting lines and is expressed in terms of the translational vector length T. We have $T = 0.46$ nm for the (23, 14) tube.

that the direct interaction K^d vanishes at $\mathbf{q} = 0$. At $\mathbf{q} = 0$, only the exchange interaction K^x gives a small contribution from the AV interaction. The vanishing K^d can be explained by the presence of three C_s^c and one C_s^v coefficients in Eq. (2). The product of wave functions always gives an opposite sign when we exchange A → B in s or s' and thus the total summation over the A and B sublattices vanishes at $\mathbf{q} = 0$ (see Appendix A). As long as we incorporate three C^c and one C^v coefficients into K^d, the vanishing direct Coulomb interaction at $\mathbf{q} = 0$ is a general phenomenon in graphene and SWNT systems. The results from Figs. 2(d) and 2(e) thus imply that the first-order Raman processes corresponding to the AV and EV interactions at $\mathbf{q} = 0$ make only minor contributions to the Raman spectra. Consequently, we should consider the second-order ERS process, in which the $\mathbf{q} \neq 0$ term in K^d becomes important. It is important to note that in K^d, the dominant matrix elements arise from $q \approx \pm 0.1\pi/T$, which is only 5% of the cutting line length and thus the transition is almost vertical. In this case, the almost vertical transition will give a similar Fermi energy dependence to that which is supposed to be happening for $\mathbf{q} = 0$.[23]

III. RESULTS AND DISCUSSION

Next, to explain the Fano resonance in mSWNTs, we calculate the Raman intensity by taking into account each contribution from the RBM, ERS, and G bands. Here we also consider that the G band consists of two distinct phonon modes, namely the in-plane transverse optic (iTO) and longitudinal optic (LO) modes. Summing up all possible initial (i) and
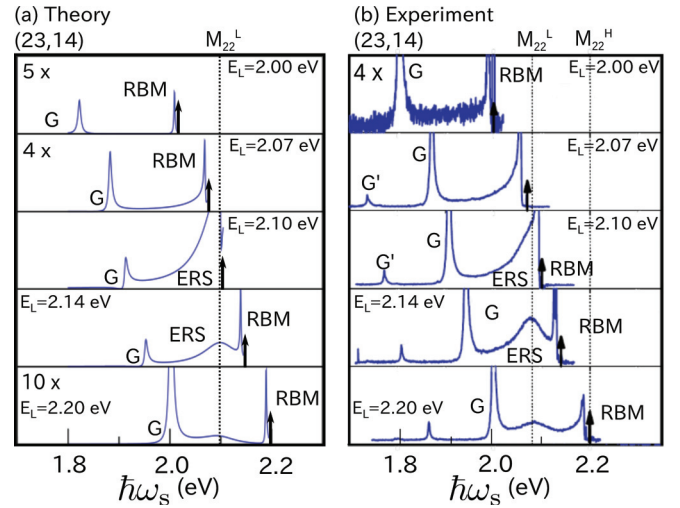
FIG. 3. (Color online) (a) Calculated result (this work) and (b) experimental results (adapted from Ref. 23) for the Raman intensity versus scattered photon energy $\hbar\omega_s$ for a (23,14) tube where we have the calculated $M_{22}^L = 2.10$ eV, and the experimental $M_{22}^L = 2.08$ eV and $M_{22}^H = 2.20$ eV. Here M_{22}^L and M_{22}^H are the splitting of the transition energy in mSWNTs due to the trigonal warping effect.[5] The laser excitation energies E_L are taken as 2.00, 2.07, 2.10, 2.14, and 2.20 eV.

final (f) states, we express the Raman intensity as[26]

$$ I = \sum_i \left| \sum_f (A_{\mathrm{RBM}} + A_{\mathrm{ERS}} + A_G) \right|^2, \qquad (7) $$

where A_{RBM} and $A_G = A_{\mathrm{iTO}} + A_{\mathrm{LO}}$ are the phonon spectral amplitudes, and A_{ERS} is the electronic scattering amplitude (see Appendix C). We do not consider the G' band because its position ($\sim$2700 cm^{-1}) is quite far from the ERS and might not interfere with the ERS, as indicated in Farhat's experiment [Fig. 3(b)].

In Fig. 3(a) we show the calculated result of the E_L dependence of the Raman intensity as a function of $\hbar\omega_s$. In the present work, we only calculate the E_L dependence of the Raman intensity near M_{22}^L with some fitting parameters for the spectral linewidth, which can be found in Appendix C. We cannot reproduce exactly the relative intensity scale in Fig. 3(a) with that of the experimental data in Fig. 3(b) because there are many optical processes interfering with these spectra other than ERS, G, and RBM. Nevertheless, our calculated result can explain the behavior of the observed ERS as shown in Fig. 3(b). The ERS feature has a very broad spectral width (FWHM$^{\mathrm{ERS}} \approx 50$ meV) with a peak intensity almost comparable to that of the RBM. Unlike the other phonon modes, whose peak positions are shifted by changing E_L, the ERS peak remains at the frequency of the M_{ii} transition. At $E_L = 2.07$ eV, the ERS spectrum starts to appear and modifies the RBM and the G-band line shapes. At that point, although E_L is 30 meV below M_{ii}, the energy-momentum conservation during the exciton-exciton scattering process may be violated by the Heisenberg uncertainty principle ($\Delta t \approx 10$ fs corresponding to $\Delta E \approx 100$ meV).

Each Raman intensity calculated from Eq. (7) actually gives a Lorentzian shape for all phonon modes and also for the ERS
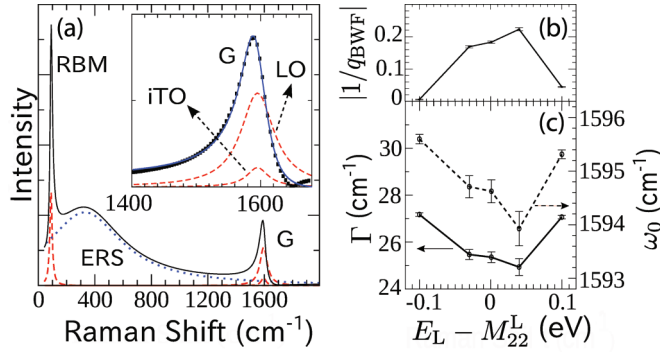
FIG. 4. (Color online) (a) Calculated Raman spectra for a (23,14) SWNT with $E_L = 2.14$ eV. The total intensity shown is represented by the solid line. The dashed lines show contributions from the RBM and G modes, while the dotted blue line is the contribution from the ERS. Each line shape for the RBM, the G modes, and the ERS is Lorentzian. The inset shows the G-band spectra after subtracting the ERS spectrum. Filled squares are calculated results and the solid line shows the BWF fitting [Eq. (8)]. (b) The asymmetric factor ($1/q_{BWF}$), and (c) spectral width (Γ) and peak position (ω_0) of the G band as a function of resonance condition ($E_L - M_{22}^L$) for the (23,14) tube. The solid and dashed arrows are given as a guide for the corresponding axes.

as presented in Fig. 4(a). However, the broad feature of the ERS overlaps with the phonon modes and thus the interference between them gives rise to the asymmetric line shape, peak shifting, and the enhancement of the G band, which can be seen in the inset of Fig. 4(a). We find that the asymmetric line shape of the G band after subtracting the ERS contribution clearly shows the BWF line shape, fitted by

$$I(\omega) = I_0 \frac{[1 + (\omega - \omega_0)/q_{BWF}\Gamma]^2}{1 + [(\omega - \omega_0)/\Gamma]^2}, \tag{8}$$

where q_{BWF}, Γ, and ω_0 are parameters to be determined. From this fitting, we can find and analyze the E_L dependence of the asymmetric factor $1/q_{BWF}$, the spectral width Γ, and the peak position ω_0 [see Figs. 4(b) and 4(c)]. According to Fano,[17] $1/q_{BWF}$ is proportional to the coupling constant between the continuum spectrum and the discrete spectrum. In our case, $|1/q_{BWF}|$ (Γ or ω_0), as a function of $E_L - M_{22}^L$, has a "Λ" ("V") shape, with the maximum (minimum) peak $\sim$40 meV above the resonance, as depicted in Fig. 4(b) [Fig. 4(c)]. Moreover, $|1/q_{BWF}|$ reaches a maximum value because the intensity and the peak position of the ERS allows it to have a very strong overlap with the G band at that point. This coupling also induces the narrowing [Fig. 4(c), left y-axis label] and the shifting of the G-band peak [Fig. 4(c), right y-axis label] closer to the ERS peak position.

In this study, we do not calculate the d_t dependence of $1/q_{BWF}$, which was discussed experimentally by Ref. 15. The reason is that the $1/q_{BWF}$ is very sensitive to the relative energy separation between M_{ii} and E_L [see Fig. 4(b)]. Thus, in order to study $1/q_{BWF}$ dependence of d_t, the E_L and chiral index (n,m) should be well-defined in the experiment. However, Ref. 15 did not discuss either the E_L dependence of $1/q_{BWF}$ or the characterization of (n,m) for their SWNTs since their samples are SWNT bundles, and thus we cannot compare the calculated result with Ref. 15. If we discuss the d_t dependence

of $1/q_{BWF}$ we need to define the E_L values relative to M_{ii} for each mSWNTs. This d_t dependence of $1/q_{BWF}$ will be discussed elsewhere.

From our theoretical point of view, we predict that the ERS, which originates from nonzero **q**, should be suppressed in a very short mSWNT ($L \approx 50$ nm). The discrete k point arises due to the finite length of the nanotube, which will prevent the nonvertical transition from satisfying the energy-momentum conservation. Therefore, to observe the ERS intensity, a typical length of the mSWNTs should be more than 1 μm. We also suggest additional conditions as to how the ERS and asymmetric phonon modes in mSWNTs can best be observed experimentally. Since the Coulomb interaction is inversely proportional to d_t and since a curvature-induced band gap ($\sim \cos\theta/d_t^2$ meV) appears for small chiral angles θ for $d_t < 1$ nm,[27] the d_t range of mSWNTs that allows us to observe the ERS and Fano resonance should be around 1–2 nm. The energy of the second-order exciton-exciton interaction is only $\sim$10 meV lower than the first-order process because the linear band slope is steeper than that of the parabolic band. Therefore, in order to identify the dominant contribution of the second-order process, a low-temperature (10–100 K) gate voltage experiment must be performed. In addition, we expect that the RBM spectra should exhibit a similar BWF asymmetry as that shown in the G band due to interference with the ERS. This phenomenon is open for future clarifications.

IV. SUMMARY

We have formulated a theoretical picture of the ERS by considering the exciton-exciton interaction. We have shown that in the direct Coulomb interaction, the zero-momentum transfer process **q** = 0 vanishes due to the symmetry properties of the SWNT sublattices. We found that this fact is a general phenomenon occurring not only in carbon sp^2 systems, but also in any material that has the same symmetry. Furthermore, by considering a **q** $\neq$ 0 second-order process, we can consistently reproduce theoretically the ERS spectra from experiment as a function of E_L. This ERS spectrum is strongly coupled with the G band and the interference with the ERS spectrum shows a BWF line shape for the G band. The asymmetry, narrowing, and frequency shifting of the G band induced by the interference with the ERS are all sensitive to the peak intensity ratio I_G/I_{ERS} and the peak distance between the ERS and the G band ($E_L - M_{ii}$).

APPENDIX A: CALCULATION OF THE ELECTRON-ELECTRON INTERACTION MATRIX ELEMENT

Here we analytically show that for the electron-electron interaction between the photoexcited electron and the linear

band electron, the direct interaction K^d vanishes at $\mathbf{q} = 0$ (and thus the exciton-exciton matrix element for the direct interaction also becomes zero). This is not due to the exciton effect but simply comes about because of symmetry considerations. The direct interaction K^d already vanishes by considering the symmetry of the A and B sublattices, before taking into account the summation on $\mathbf{k}$ weighted by the exciton wave function $Z_\mathbf{k}$ [see Eqs. (2) and (4) in the main paper]. The interaction between an electron in the parabolic-band and an electron in the linear band of a metallic single-wall carbon nanotube (mSWNT) without the screening effect is given by

$$V_{1,2,3,4}^{(\pm)} = \int d\mathbf{r}d\mathbf{r}' \Phi_{12}^{*(\pm)}(\mathbf{r},\mathbf{r}')\frac{e^2}{|\mathbf{r}-\mathbf{r}'|}\Phi_{34}^{(\pm)}(\mathbf{r},\mathbf{r}'), \quad \text{(A1)}$$

where $(1,2,3,4) = (\mathbf{k}_1 a_1, \mathbf{k}_2 a_2, \mathbf{k}_3 a_3, \mathbf{k}_4 a_4)$ corresponds to $\{(\mathbf{k}+\mathbf{q})_c, (\mathbf{k}'-\mathbf{q})_c, \mathbf{k}_c, \mathbf{k}'_v\}$ in Eq. (1), a_i denotes either c (conduction) or v (valence) band states, and $\mathbf{k}$ ($\mathbf{k}'$) is an electronic wave vector for the parabolic (linear) band. In the case of SWNTs, the allowed wave vectors are on the so-called cutting lines and can be expressed by $\mathbf{k} = \mu\mathbf{K}_1 + k\mathbf{K}_2/|\mathbf{K}_2|$, where $\mu = 0,1,...,N-1$ and $-\pi/T \leqslant k \leqslant \pi/T$.[28] Vectors $\mathbf{K}_1$ and $\mathbf{K}_2$ are the reciprocal lattice vectors along the circumferential and axial directions, respectively, while N and T are the number of hexagons in a SWNT unit cell and the length of the translational vector, respectively.

The two-body wave function $\Phi_{i,j}^{(\pm)}(\mathbf{r},\mathbf{r}')$ is defined as

$$\Phi_{i,j}^{(\pm)}(\mathbf{r},\mathbf{r}') = \frac{1}{\sqrt{2}}[\psi_i(\mathbf{r})\psi_j(\mathbf{r}') \pm \psi_i(\mathbf{r}')\psi_j(\mathbf{r})], \quad \text{(A2)}$$

with $i,j = 3,4$ ($i,j = 1,2$) denoting the initial (final) state, where the parabolic band electron lies around the $\mathbf{k}_3 a_3$ ($\mathbf{k}_1 a_1$) state and the linear band electron lies around $\mathbf{k}_4 a_4$ ($\mathbf{k}_2 a_2$). The $+(-)$ sign is taken for the spin singlet (triplet) state. Substituting Eq. (A2) into Eq. (A1), we obtain

$$V_{1,2,3,4}^{(\pm)} = K^d \pm K^x, \quad \text{(A3)}$$

where

$$K^d = \tfrac{1}{2}\{K_{1,2,3,4} + K_{2,1,4,3}\} \quad \text{(A4)}$$

$$K^x = \tfrac{1}{2}\{K_{1,2,4,3} + K_{2,1,3,4}\}, \quad \text{(A5)}$$

and

$$K_{1,2,3,4} = \int d\mathbf{r}d\mathbf{r}' \psi_1^*(\mathbf{r})\psi_2^*(\mathbf{r}')\frac{e^2}{|\mathbf{r}-\mathbf{r}'|}\psi_3(\mathbf{r})\psi_4(\mathbf{r}'). \quad \text{(A6)}$$

Now the one-electron wave function ψ_i can be explicitly written as a linear combination of atomic orbitals in a unit cell:

$$|\psi_i(\mathbf{r})\rangle = |\mathbf{k}_i a_i\rangle = C_{A,\mathbf{k}_i}^{a_i}|A\rangle + C_{B,\mathbf{k}_i}^{a_i}|B\rangle, \quad \text{(A7)}$$

where the atomic site wave function $\{|s\rangle, \ s \in (A \text{ or } B)\}$ is given by a Bloch function

$$|s\rangle = \frac{1}{\sqrt{N}}\sum_{u=1}^N e^{i\mathbf{k}\cdot\mathbf{R}_{us}}|\phi(\mathbf{r}-\mathbf{R}_{us})\rangle, \quad \text{(A8)}$$

where $\mathbf{R}$ is the atomic position, and $\phi(\mathbf{r}-\mathbf{R})$ is the atomic orbital. The coefficient $C_{s,\mathbf{k}}^a$ is obtained from a tight binding
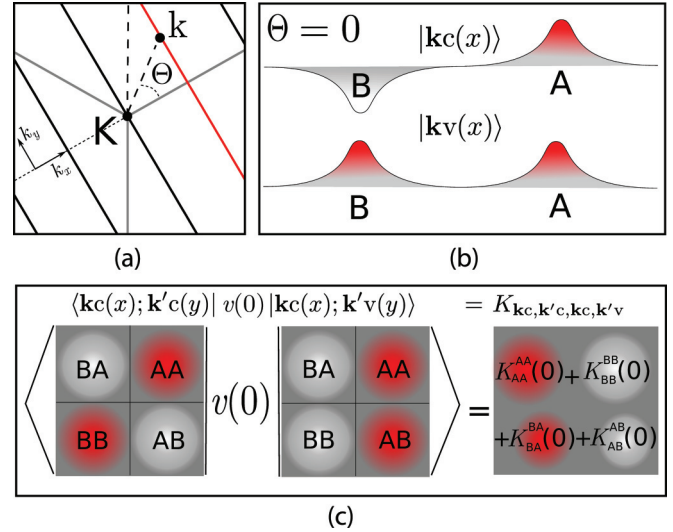
FIG. 5. (Color online) (a) The phase factor $\Theta(\mathbf{k}) = \arctan(k_y/k_x)$ in Eq. (A9) where k_x (k_y) axis is defined by circumferential (axis) direction of a zigzag SWNT.[29] (b) Schematic figure of one-body electron wave functions at $|\mathbf{k}c\rangle$ and $|\mathbf{k}v\rangle$ as defined by Eq. (A7). For simplicity, we plot the atomic orbitals only along a one-dimensional line connecting the A and B atoms (x axis). (c) Schematic figure of the Coulomb integral Eq. (A11) $K_{\mathbf{k}c,\mathbf{k}'c,\mathbf{k}c,\mathbf{k}'v}$ at $\mathbf{q} = 0$. The two-body wavefunction $|\mathbf{k}a(x);\mathbf{k}'b(y)\rangle$, $(a, b = c, v)$ is substituted from (b). Generally, $|v_{ss}(0)| > |v_{ss'}(0)|$ with $[s,s' \in (A \text{ or } B), s' \neq s]$ as defined in Eq. (A12). The red (white) color shows a positive (negative) value. From the approximation in Eq. (A11), the dominant matrix elements constituting $K_{\mathbf{k}c,\mathbf{k}'c,\mathbf{k}c,\mathbf{k}'v}$ come from the diagonal part.

method. Evaluating $C_{s,\mathbf{k}}^a$ near the K and K' point, we get

$$C_{A,\mathbf{K}+\mathbf{k}}^c = \frac{1}{\sqrt{2}}, \quad C_{B,\mathbf{K}+\mathbf{k}}^c = -\frac{1}{\sqrt{2}}e^{-i\Theta(\mathbf{k})},$$

$$C_{A,\mathbf{K}+\mathbf{k}}^v = \frac{1}{\sqrt{2}}, \quad C_{B,\mathbf{K}+\mathbf{k}}^v = \frac{1}{\sqrt{2}}e^{-i\Theta(\mathbf{k})},$$

$$C_{A,\mathbf{K}'+\mathbf{k}}^c = \frac{1}{\sqrt{2}}, \quad C_{B,\mathbf{K}'+\mathbf{k}}^c = \frac{1}{\sqrt{2}}e^{i\Theta(\mathbf{k})}, \quad \text{(A9)}$$

$$C_{A,\mathbf{K}'+\mathbf{k}}^v = \frac{1}{\sqrt{2}}, \quad C_{B,\mathbf{K}'+\mathbf{k}}^v = -\frac{1}{\sqrt{2}}e^{i\Theta(\mathbf{k})},$$

where $\Theta(\mathbf{k}) = \arctan(k_y/k_x)$ is measured from the K or K' points [see Fig. 5(a)], vectors corresponding to the K and K' points are denoted by $\mathbf{K}$ and $\mathbf{K}'$, respectively.[12] The shape of the $|\mathbf{k}a\rangle$ wavefunctions near the K point at $\Theta(\mathbf{k}) = 0$ show an antisymmetric (symmetric) function under the $A \to B$ exchange for $|\mathbf{k}c\rangle$ ($|\mathbf{k}v\rangle$), as illustrated in Fig. 5(b).

Substituting Eq. (A7) into Eq. (A6), we get

$$K_{1,2,3,4} = \frac{1}{N^2}\sum_{s_1 u_1, s_2 u_2}\left[\sum_{s_1' u_1', s_2' u_2'} C_{s_1,\mathbf{k}_1}^{a_1*} C_{s_1',\mathbf{k}_2}^{a_2*} C_{s_2,\mathbf{k}_3}^{a_3} C_{s_2',\mathbf{k}_4}^{a_4}\right.$$

$$\times e^{-i(\mathbf{k}_1\cdot\mathbf{R}_{u_1 s_1} + \mathbf{k}_2\cdot\mathbf{R}_{u_1' s_1'} - \mathbf{k}_3\cdot\mathbf{R}_{u_2 s_2} - \mathbf{k}_4\cdot\mathbf{R}_{u_2' s_2'})}$$

$$\times \int d\mathbf{r}d\mathbf{r}' \phi(\mathbf{r}-\mathbf{R}_{u_1 s_1})\phi(\mathbf{r}'-\mathbf{R}_{u_1' s_1'})$$

$$\left. \times \frac{e^2}{|\mathbf{r}-\mathbf{r}'|}\phi(\mathbf{r}-\mathbf{R}_{u_2 s_2})\phi(\mathbf{r}'-\mathbf{R}_{u_2' s_2'})\right]. \quad \text{(A10)}$$

The largest contribution from the integrand in Eq. (A10) comes from $(u_1 s_1) = (u_2 s_2) \equiv (us)$ and $(u_1' s_1') = (u_2' s_2') \equiv (u's')$. Thus, we can obtain

$$
\begin{aligned}
K_{1,2,3,4} \cong{}& \delta(\mathbf{k_3} + \mathbf{k_4}, \mathbf{k_1} + \mathbf{k_2}) \\
&\times \sum_{ss'} C_{s,\mathbf{k_1}}^{a_1*} C_{s',\mathbf{k_2}}^{a_2*} C_{s,\mathbf{k_3}}^{a_3} C_{s',\mathbf{k_4}}^{a_4} v_{ss'}(\mathbf{k_4} - \mathbf{k_2}),
\end{aligned}
$$
$$(A11)$$

where

$$
\begin{aligned}
v_{ss'}(\mathbf{q}) ={}& \frac{1}{N} \sum_{u'} e^{i\mathbf{q}\cdot(\mathbf{R}_{u's'} - \mathbf{R}_{0s})} \int d\mathbf{r} d\mathbf{r}' \frac{e^2}{|\mathbf{r} - \mathbf{r}'|} \\
&\times |\phi(\mathbf{r} - \mathbf{R}_{0s})|^2 |\phi(\mathbf{r}' - \mathbf{R}_{u's'})|^2,
\end{aligned}
$$
$$(A12)$$

is the Fourier transform of the Coulomb potential. We define the integration of Eq. (A12) as $v_{ss'}(\mathbf{q})$,

$$
v_{ss'}(\mathbf{q}) = \frac{1}{N} \sum_{u'} e^{i\mathbf{q}\cdot(\mathbf{R}_{u's'} - \mathbf{R}_{0s})} v(\mathbf{R}_{0s}, \mathbf{R}_{u's'}),
$$
$$(A13)$$

where $v(\mathbf{R}, \mathbf{R}')$ is the effective Coulomb potential for the π electron system modeled by the Ohno potential:

$$
v(\mathbf{R}, \mathbf{R}') = \frac{U_0}{\sqrt{\left(\frac{4\pi\epsilon_0}{e^2} U_0 |\mathbf{R} - \mathbf{R}'|\right)^2 + 1}},
$$
$$(A14)$$

in which U_0 is the on-site Coulomb potential for two π electrons at the same site $\mathbf{R} = \mathbf{R}'$, defined by[6,30]

$$
U_0 = \int d\mathbf{r} d\mathbf{r}' \frac{e^2}{|\mathbf{r} - \mathbf{r}'|} \phi_\pi^2(\mathbf{r}) \phi_\pi^2(\mathbf{r}') = 11.3 \text{ eV}.
$$
$$(A15)$$

The lower energy level of the exciton in SWNTs is well-described by this Ohno potential.[31] We can show that $v_{AA}(\mathbf{q}) = v_{BB}(\mathbf{q})$ and $v_{AB}(\mathbf{q}) = v_{BA}^*(\mathbf{q})$ because of the symmetry between the A and B sublattices. The corresponding direct and exchange terms from Eqs. (A4) and (A5) are now expressed by

$$
\begin{aligned}
K^d ={}& \frac{1}{2} \left\{ K_{(\mathbf{k+q})_c, (\mathbf{k'-q})_c, \mathbf{k}_c, \mathbf{k}_v'} + K_{(\mathbf{k'-q})_c, (\mathbf{k+q})_c, \mathbf{k}_v', \mathbf{k}_c} \right\} \\
={}& \sum_{ss'=A,B} C_{s,\mathbf{k+q}}^{c*} C_{s',\mathbf{k'-q}}^{c*} C_{s,\mathbf{k}}^{c} C_{s',\mathbf{k'}}^{v} \mathrm{Re}[v_{ss'}(\mathbf{q})],
\end{aligned}
$$
$$(A16)$$

$$
\begin{aligned}
K^x ={}& \frac{1}{2} \left\{ K_{(\mathbf{k+q})_c, (\mathbf{k'-q})_c, \mathbf{k}_v', \mathbf{k}_c} + K_{(\mathbf{k'-q})_c, (\mathbf{k+q})_c, \mathbf{k}_c, \mathbf{k}_v'} \right\} \\
={}& \sum_{ss'=A,B} C_{s,\mathbf{k+q}}^{c*} C_{s',\mathbf{k'-q}}^{c*} C_{s',\mathbf{k}}^{c} C_{s,\mathbf{k'}}^{v} \mathrm{Re}[v_{ss'}(\mathbf{k'} - \mathbf{k} - \mathbf{q})].
\end{aligned}
$$
$$(A17)$$

Inserting Eqs. (A9) and (A13) into Eqs. (A16) and (A17), at $\mathbf{q} = 0$, the direct interaction becomes

$$
\begin{aligned}
K_{\mathbf{k+K}, \mathbf{k'+K}}^d ={}& \tfrac{1}{4} \{ \mathrm{Re}[v_{AA}(0)] - \mathrm{Re}[v_{AB}(0)] \\
&+ \mathrm{Re}[v_{BA}(0)] - \mathrm{Re}[v_{BB}(0)] \} \\
={}& 0,
\end{aligned}
$$
$$(A18)$$

which works the same for $K_{\mathbf{k+K}, \mathbf{k'+K}}^d = K_{\mathbf{k+K'}, \mathbf{k'+K}}^d = K_{\mathbf{k+K}, \mathbf{k'+K'}}^d = K_{\mathbf{k+K'}, \mathbf{k'+K'}}^d = 0$, and the exchange interaction

becomes

$$
\begin{aligned}
K_{\mathbf{k+K}, \mathbf{k'+K}}^x ={}& \frac{i}{2} \sin[\Theta'(\mathbf{k'}) - \Theta(\mathbf{k})] \mathrm{Re}[v_{AB}(\mathbf{k'} - \mathbf{k})], \\
K_{\mathbf{k+K'}, \mathbf{k'+K}}^x ={}& \frac{i}{2} \sin[\Theta'(\mathbf{k'}) + \Theta(\mathbf{k})] \mathrm{Re}[v_{AB}(\mathbf{k'} - \mathbf{k})].
\end{aligned}
$$
$$(A19)$$

The exchange interactions also give $K_{\mathbf{k+K'}, \mathbf{k'+K'}}^x = K_{\mathbf{k+K}, \mathbf{k'+K}}^{x*}$ and $K_{\mathbf{k+K}, \mathbf{k'+K'}}^x = K_{\mathbf{k+K'}, \mathbf{k'+K}}^{x*}$. Equation (A18) proves that the direct terms K^d in the first-order process at $\mathbf{q} = 0$ vanish, and only the exchange terms K^x survive. This vanishing comes from the symmetry of the sublattice wavefunction as illustrated in Fig. 5(c). The combination of three symmetric wavefunctions and one antisymmetric wavefunction (and vice versa) in the Coulomb integral Eq. (A11) leads to the antisymmetric matrix element under the $A \rightarrow B$ sublattice exchange. Thus, in K^d at $\mathbf{q} = 0$, the contribution from AA is always canceled by BB, and AB is canceled by BA [Eq. (A18)]. Although the shape of the wavefunction in Fig. 5(c) is taken only for $\Theta(\mathbf{k}) = 0$, the illustration is valid since the phase factor of the two-body wavefunction will disappear at $\mathbf{q} = 0$ due to complex conjugation. Therefore, the first-order exciton-exciton scattering process makes a very small contribution to the ERS spectra so that we must then consider the second-order process as has been described in the main paper.

If we include the screening effect, we just change $v(\mathbf{q})$ to be the screened potential $w(\mathbf{q}) = v(\mathbf{q})/\kappa[1 + v(\mathbf{q})\Pi(\mathbf{q})]$. Here, κ is the static dielectric constant due to the electronic core states, the σ band, and the surrounding materials. In this calculation, we use $\kappa = 2.2$, and $\Pi(\mathbf{q})$ is the RPA polarization function,[6] which is given by

$$
\Pi(\mathbf{q}) = -2 \sum_{\mathbf{k}, a, a'} \frac{f_{\mathbf{k+q}a'} - f_{\mathbf{k}a'}}{\epsilon_{\mathbf{k+q}a'} - \epsilon_{\mathbf{k}a}} \left| \int \psi_{\mathbf{k}a}^*(\mathbf{r}) e^{-i\mathbf{q}\cdot\mathbf{r}} \psi_{\mathbf{k+q}a'}(\mathbf{r}) d\mathbf{r} \right|^2,
$$
$$(A20)$$

with $f_{\mathbf{k}a} = 1(0)$ for the valence (conduction) bands. Here, $\epsilon_{\mathbf{k}}$ is the single-particle energy, and the summation over $\mathbf{k}$ is taken over all cutting lines in the graphene Brillouin zone.

APPENDIX B: VIRTUAL STATE APPROXIMATION

When an electron in a ground state absorbs a photon with energy E_L, an exciton is thus generated and occupies a virtual state in which the exciton energy ($=E_L$) may not be resonant with any exciton energy states. We can then define the virtual state as a linear combination of the exciton states:

$$
|\Psi^{\mathrm{vir}}\rangle = \sum_n A_n |n\rangle,
$$
$$(B1)$$

where $|n\rangle = \sum_{\mathbf{k}} Z_{\mathbf{k}c, \mathbf{k}v}^n c_{\mathbf{k}}^{\dagger c} c_{\mathbf{k}}^v |g\rangle$ is the nth exciton state and A_n is the coefficient of the transition from the ground state $|g\rangle$ to state $|n\rangle$, which is determined from the time-dependent perturbation theory (TDPT). From the TDPT calculation, we obtain

$$
A_n(E_L, t) = \sqrt{N_A} \mathcal{M}_{\mathrm{ex-op}}^{n,g} \frac{\sin(E_L - E_n)t/2\hbar}{E_L - E_n},
$$
$$(B2)$$

where N_A is the normalization constant to guarantee $\sum_n |A_n|^2 = 1$. We eliminate the time-dependency by taking the root mean square over time in the limit $\lim \tau \rightarrow \infty$. We
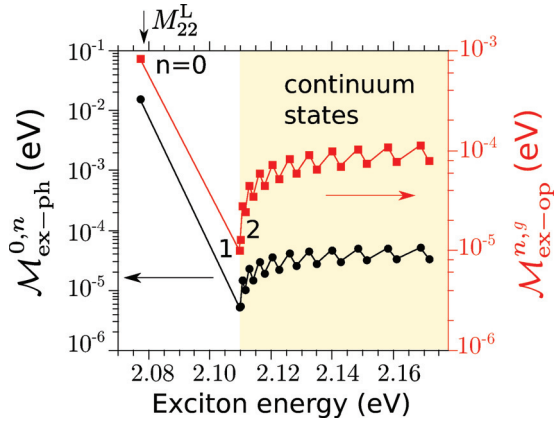
FIG. 6. (Color online) The LO exciton-phonon matrix element from the nth state to the lowest exciton state $\mathcal{M}^{0,n}_{\text{ex-ph}}$ and the exciton-photon matrix element $\mathcal{M}^{n,i}_{\text{ex-op}}$ from the initial state to the nth exciton state.[35]

then obtain the average transition probability:

$$\left\langle A_n^2(E_L)\right\rangle_\tau = N_A \left(\frac{\mathcal{M}^{n,g}_{\text{ex-op}}}{E_L - E_n - i\gamma} \right)^2, \qquad \text{(B3)}$$

where we have included a phenomenological quasiparticle lifetime $\gamma \approx 60$ meV as suggested by the experiment in Ref. 1. From Eq. (B3), we can say that the transition probability to state n is determined by the exciton-photon matrix elements and by the resonance condition of that energy state to the laser energy E_L.

In Eq. (5), we approximate the virtual state as the lowest exciton state. We can justify the approximation based on a calculation of Raman intensity resulting from each exciton state. In order to obtain the intensity contribution from each state, we use Eqs. (B1) and (B3) in Eq. (C1) for the LO mode and set $\hbar\omega_s = M^L_{22}$, assuming that in $\mathcal{M}_{\text{ex-ph}}$ a photoexcited exciton from the nth state emits a phonon and always relaxes to the lowest exciton state $n = 0$. Figure 6 shows that $\mathcal{M}^{0,n=0}_{\text{ex-ph}}$ ($\mathcal{M}^{n=0,i}_{\text{ex-op}}$) is typically three orders (one order) of magnitude larger than that in the continuum states. Therefore, the relative Raman intensity from the lowest exciton state I^0 is almost ten orders larger than that in the continuum states. Based on this result, we dismiss the contributions of the continuum exciton states to the virtual state.

APPENDIX C: CALCULATION OF THE RAMAN SPECTRA AMPLITUDES

The amplitude of the RBM and the G band can be calculated by[32,33]

$$A_\nu(\omega_s) = \frac{1}{\pi} \sum_{n,n'} \left\{ \frac{\mathcal{M}^{n,i}_{\text{ex-op}}}{[\Delta E_{ni} - i\gamma]} \right.$$

$$\times \frac{\mathcal{M}^{n',n}_{\text{ex-ph}}}{[\Delta E_{n'i} - \hbar\omega_\nu - i(\gamma + \Gamma_\nu)]}$$

$$\left. \times \frac{\mathcal{M}^{f,n'}_{\text{ex-op}}}{[E_L - \hbar\omega_\nu - \hbar\omega_s - i\Gamma_\nu]} \right\}, \qquad \text{(C1)}$$

where ν = RBM or G mode, and $\Delta E_{mi} = E_L - E_m - E_i$. We use a broadening factor $\gamma = 60$ meV for the lifetime of the photoexcited carriers.[34] We also utilize the phonon spectral width for the RBM as a constant $\Gamma_{\text{RBM}} = 10$ cm^{-1}, and for the G band, which consists of an iTO $\Gamma_{\text{iTO}} = 20$ cm^{-1} and a LO $\Gamma_{\text{LO}} = 31$ cm^{-1}.[21] The exciton-photon ($\mathcal{M}^{b,a}_{\text{ex-op}}$) and exciton-phonon ($\mathcal{M}^{b,a}_{\text{ex-ph}}$) matrix elements for a transition between states $a \rightarrow b$ are taken from Jiang's work.[35] We approximate the virtual states $i = f$ and $n = n'$. On the other hand, the amplitude of the second-order ERS process is given by[32,33]

$$A_{\text{ERS}}(\omega_s) = \frac{1}{\pi} \sum_{n,n',n'',\sigma} \left\{ \frac{\mathcal{M}^{n,i}_{\text{ex-op}}}{[\Delta E_{ni} - i\gamma]} \right.$$

$$\times \frac{\mathcal{M}^{n',n}_{\text{ex-ex}}(q)}{[\Delta E_{n'i} - \hbar\omega_1 - i(\gamma + \Gamma_x)]}$$

$$\times \frac{\mathcal{M}^{n'',n'}_{\text{ex-ex}}(-q)}{[\Delta E_{n''i} - \hbar\omega_1 - \hbar\omega_2 - i(\gamma + 2\Gamma_x)]}$$

$$\left. \times \frac{\mathcal{M}^{f,n'}_{\text{ex-op}}}{[E_L - \hbar\omega_1 - \hbar\omega_2 - \hbar\omega_s - 2i\Gamma_x]} \right\}, \qquad \text{(C2)}$$

where we also consider the same virtual state approximation as in Eq. (C1). Here, ω_1 and ω_2 are the energies of the linear band excitons emitted from the exciton-exciton interaction in the second-order ERS process. The summation over σ denotes all different processes in the ERS mechanism, i.e., the intravalley (AV) and intervalley (EV) interactions as shown in Fig. 1. The electron-electron interaction lifetime is assumed to have a constant value $\Gamma_x = 25$ meV so as to reproduce the experimental ERS spectral width.

*hasdeo@flex.phys.tohoku.ac.jp

[1]R. Saito, M. Hofmann, G. Dresselhaus, A. Jorio, and M. S. Dresselhaus, Adv. Phys. **60**, 413 (2011).

[2]A. Jorio, R. Saito, J. H. Hafner, C. M. Lieber, M. Hunter, T. McClure, G. Dresselhaus, and M. S. Dresselhaus, Phys. Rev. Lett. **86**, 1118 (2001).

[3]A. M. Pimenta, A. Marucci, S. D. M. Brown, M. J. Mattews, A. M. Rao, P. C. Eklund, R. E. Smalley, G. Dresselhaus, and M. S. Dresselhaus, J. Mater. Res. **13**, 2396 (1998).

[4]H. Kataura, Y. Kumazawa, Y. Maniwa, I. Umezu, S. Suzuki, Y. Ohtsuka, and Y. Achiba, Synth. Met. **103**, 2555 (1999).

[5]R. Saito, G. Dresselhaus, and M. S. Dresselhaus, Phys. Rev. B **61**, 2981 (2000).

[6]J. Jiang, R. Saito, Ge. G. Samsonidze, A. Jorio, S. G. Chou, G. Dresselhaus, and M. S. Dresselhaus, Phys. Rev. B **75**, 035407 (2007).

[7]H. Farhat, H. Son, Ge. G. Samsonidze, S. Reich, M. S. Dresselhaus, and J. Kong, Phys. Rev. Lett. **99**, 145506 (2007).

[8]K. I. Sasaki, R. Saito, G. Dresselhaus, M. S. Dresselhaus, H. Farhat, and J. Kong, Phys. Rev. B **78**, 235405 (2008).

[9]J. S. Park, K. Sasaki, R. Saito, W. Izumida, M. Kalbac, H. Farhat, G. Dresselhaus, and M. S. Dresselhaus, Phys. Rev. B **80**, 081402 (2009).

[10] S. Uryu and T. Ando, Phys. Rev. B **74**, 155411 (2006).

[11] Y. Miyauchi, M. Oba, and S. Maruyama, Phys. Rev. B **74**, 205440 (2006).

[12] A. Grüneis, R. Saito, Ge. G. Samsonidze, T. Kimura, M. A. Pimenta, A. Jorio, A. G. Souza Filho, G. Dresselhaus, and M. S. Dresselhaus, Phys. Rev. B **67**, 165402 (2003).

[13] L. Li, T. Chang, and G. Li, Carbon **49**, 4412 (2011).

[14] S. B. Cronin, A. K. Swan, M. S. Ünlü, B. B. Goldberg, M. S. Dresselhaus, and M. Tinkham, Phys. Rev. B **72**, 035425 (2005).

[15] S. D. M. Brown, A. Jorio, P. Corio, M. S. Dresselhaus, G. Dresselhaus, R. Saito, and K. Kneipp, Phys. Rev. B **63**, 155414 (2001).

[16] P. C. Eklund, G. Dresselhaus, M. S. Dresselhaus, and J. E. Fischer, Phys. Rev. B **16**, 3330 (1977).

[17] U. Fano, Phys. Rev. **124**, 1866 (1961).

[18] S. M. Bose, S. Gayen, and S. N. Behera, Phys. Rev. B **72**, 153402 (2005).

[19] C. Jiang, K. Kempa, J. Zhao, U. Schlecht, U. Kolb, T. Basché, M. Burghard, and A. Mews, Phys. Rev. B **66**, 161404 (2002).

[20] K. Kempa, Phys. Rev. B **66**, 195406 (2002).

[21] M. Lazzeri, S. Piscanec, Francesco Mauri, A. C. Ferrari, and J. Robertson, Phys. Rev. B **73**, 155426 (2006).

[22] Y. Wu, J. Maultzsch, E. Knoesel, B. Chandra, M. Huang, M. Y. Sfeir, L. E. Brus, J. Hone, and T. F. Heinz, Phys. Rev. Lett. **99**, 027402 (2007).

[23] H. Farhat, S. Berciaud, M. Kalbac, R. Saito, T. F. Heinz, M. S. Dresselhaus, and J. Kong, Phys. Rev. Lett. **107**, 157401 (2011).

[24] F. Wang, D. J. Cho, B. Kessler, J. Deslippe, P. J. Schuck, S. G. Louie, A. Zettl, T. F. Heinz, and Y. R. Shen, Phys. Rev. Lett. **99**, 227401 (2007).

[25] C. D. Spataru, S. Ismail-Beigi, L. X. Benedict, and S. G. Louie, Phys. Rev. Lett. **92**, 077402 (2004).

[26] J. Friedman and R. M. Hochstrasser, Chem. Phys. Lett. **32**, 414 (1975).

[27] M. Ouyang, J. L. Huang, C. L. Cheung, and C. M. Lieber, Science **292**, 702 (2001).

[28] Ge. G. Samsonidze, R. Saito, A. Jorio, M. A. Pimenta, A. G. Souza Filho, A. Grüneis, G. Dresselhaus, and M. S. Dresselhaus, J. Nanosci. Nanotech. **3**, 431 (2003).

[29] K. Sasaki and R. Saito, Prog. Theor. Phys. **176**, 253 (2008).

[30] V. Perebeinos, J. Tersoff, and P. Avouris, Phys. Rev. Lett. **92**, 257402 (2004).

[31] R. B. Capaz, C. D. Spataru, S. Ismail-Beigi, and S. G. Louie, Phys. Rev. B **74**, 121401 (2006).

[32] A. Jorio, M. Dresselhaus, R. Saito, and G. Dresselhaus, *Raman Spectroscopy in Graphene and Related Systems* (Wiley, New York, 2011).

[33] P. Yu and M. Cardona, *Fundamentals of Semiconductors—Physics and Material Properties* (Springer, Berlin, 2010).

[34] K. Sato, R. Saito, A. R. T. Nugraha, and S. Maruyama, Chem. Phys. Lett. **497**, 94 (2010).

[35] J. Jiang, R. Saito, K. Sato, J. S. Park, Ge. G. Samsonidze, A. Jorio, G. Dresselhaus, and M. S. Dresselhaus, Phys. Rev. B **75**, 035405 (2007).